International Journal of Impact Engineering 176 (2023) 104552

Contents lists available at ScienceDirect

International Journal of Impact Engineering

journal homepage: www.elsevier.com/locate/ijimpeng

Dynamic behavior and thermomechanical characterization of laser powder bed fusion and wrought Ti–6Al–4V

Seyyed-Danial Salehi, Roger Beal, Owen T. Kingstedt *

Department of Mechanical Engineering, University of Utah, Salt Lake City, UT, 84112, USA

ARTICLE INFO

Keywords:
Split Hopkinson pressure bar
Taylor–Quinney coefficient
Schwarzschild optical system
Laser powder bed fusion Ti–6Al–4V
Thermomechanics

ABSTRACT

In this work, the high-strain-rate stress–strain behavior and plastic work to heat conversion efficiency, also known as the Taylor–Quinney coefficient (TQC), of wrought and laser powder bed fusion (LPBF) additively manufactured Ti–6Al–4V is investigated. A double Schwarzschild optical system, designed with the use of maximizing an objective function, and IR detector are paired to achieve a high signal-to-noise ratio when monitoring real-time specimen temperature rise during high-strain-rate specimen deformation. Adiabatic deformation conditions were achieved using a split-Hopkinson tension bar. Three Ti–6Al–4V material conditions were examined, specifically rolled Ti–6Al–4V sheet (grade 5) in an annealed state, stress-released LPBF Ti–6Al–4V subjected to an annealing heat treatment exceeding the β-phase transus temperature, and LPBF Ti–6Al–4V subjected to a sawtooth profile heat treatment below the β-phase transus temperature. Electron back scattered diffraction was employed to investigate grain size and morphology, texture, and phase distribution. Wrought Ti–6Al–4 was found to have small 5 μm diameter equiaxed grains. Stress-released LPBF Ti–6Al–4V was observed to consist of lenticular grains with large aspect ratios. Lastly, the sawtooth heat treatment presented a weak bi-modal structure due to the incomplete globularization of lenticular grains. The TQC as a function of plastic strain is presented for each material system. It was found that the wrought material condition had the lowest TQC ($\beta \approx 0.35$) among the material states examined. The sawtooth heat treatment resulted in an intermediate TQC ($\beta \approx 0.52$), and the annealed heat treatment had the largest TQC ($\beta \approx 0.75$).

1. Introduction

Titanium alloys, particularly Ti–6Al–4V, is a desirable material in many industrial applications, especially aerospace, due to its high strength-to-weight ratio. Additionally, its excellent corrosion resistance and biocompatibility make it a strong candidate for medical components such as hip replacements. Ti–6Al–4V has been tailored to achieve a good balance of favorable properties including strength, ductility, fracture toughness, high-temperature strength, creep characteristics, weldability, workability, and thermal processability (e.g., higher strength is easily obtained through heat treatment) [1]. The high strength of Ti–6Al–4V originates from solid solution strengthening imparted by the hexagonal-close-packed (hcp) α-phase, whereas ductility and toughness are attributed to the body-centered-cubic (bcc) β-phase [2].

Conventional Ti–6Al–4V products rely on forging, casting, and rolling of bulk feedstock material followed by subsequent machining to final shape and dimensions, resulting in a large amount of material waste, high manufacturing cost and long lead times [3]. Conversely, additive manufacturing (AM) involves the fabrication of complex components with high degrees of geometrical freedom in an expedited production time without the need for expensive tooling (e.g., dies and cast molds) [2]. Selective laser melting (SLM) is a laser powder-bed-fusion (LPBF) AM process whereby a high-density-focused laser beam selectively scans a powder bed and those scanned and solidified layers are stacked upon each other to build a fully functional three-dimensional part, tool, or prototype [4]. The favorable weldability characteristics of Ti–6Al–4V has resulted in it becoming one of the preeminent additively manufactured alloys, particularly through the use of LPBF.

LPBF is a complicated metallurgical process, which involves powder melting, rapid directional solidification, re-melting, and re-solidification during the subsequent scan tracks, layering, and post-solidification thermal cycling [5]. The directional heat dissipation during LPBF often causes epitaxial grain growth and, thus, strong crystallographic texture, which results in mechanical property anisotropy [6–8]. When the laser heats the powder bed, the grains in the previous deposited layers and the top layer of powder transforms into the β-phase, which then solidifies and grows along the direction of heat

* Corresponding author.
E-mail address: o.kingstedt@utah.edu (O.T. Kingstedt).

https://doi.org/10.1016/j.ijimpeng.2023.104552
Received 11 August 2022; Received in revised form 3 November 2022; Accepted 27 February 2023
Available online 7 March 2023

conduction, typically with a columnar morphology oriented with build direction. As the laser rasters across the powder bed, multiple α'-phase martensitic laths precipitate within the elongated columnar grain of the parent β-phase grain [7]. The α'-phase martensitic laths are brittle increasing yield stress slightly, but greatly reducing ductility with elongation values typically less than 10% which is undesirable for most industrial applications [9].

Post processing heat treatments are applied to decompose the α'-phase martensitic laths into α-phase and β-phase laths and to transform the columnar β-phase grains into lamellar $\alpha + \beta$-phase grains which improve ductility. The martensitic α'-phase laths significantly decomposes to α-phase and β-phase laths after 20 min at 800 °C [10]. When heating below the β-phase transus of 995 °C, features of the original microstructure are maintained, but above the β-phase transus of 995 °C, a fully homogenic, 100% β-phase microstructure exists at high temperature, and during furnace cooling, a lamellar $\alpha + \beta$-phase mixture is formed [11].

In general, LPBF produced parts has a much higher surface roughness parameter R_a than the surface of a conventionally manufactured wrought part. The increased R_a is largely due to a staircase step edge on the surface from the layer wise production sequence [12,13]. The surface roughness of as-built components must be corrected through subtractive machining techniques such as machining, milling and polishing to obtain a quality surface, which adds time and cost to the overall manufacturing process. Previous work has demonstrated that surface roughness is detrimental to fatigue strength, with the fatigue strength of as-built components being as low as one third that of the ideal fatigue strength [14]. Tight tolerances and strict surface integrity requirements are not yet achievable when employing standalone AM technologies and therefore, require post-processing to meet requirements associated with surface finish, dimensional tolerances and mechanical properties. An innovative solution to improving AM surface quality is the advent of hybrid AM which consists of a laser scan followed by a machining step [15]. In this hybrid AM process, the external defects of AM parts can be removed via in-situ machining, and can be done simultaneously or in succession, eliminating the need for time consuming post processing steps [16].

The unique tribological contact phenomenon associated with machining, is highly localized, non-linear, occurs at high temperatures, high pressures, and high strains, making it extremely difficult to predict or assess the performance of various models developed for modeling machining process [17]. The very high strain-rates that occur during machining processes require an understanding of the self heating that occurs during deformation [18] as well as understanding of situations during which localized failure processes initiate (e.g., adiabatic shear band formation). The focus of the presented work is the temperature rise associated with plasticity. Previous efforts that have focused on adiabatic shear band formation can be found elsewhere [19,20].

During deformation, metals store some energy in their microstructure through deformation mechanisms such as dislocations and deformation twinning while the remainder is converted to heat. When deformation occurs at high strain-rates the heat generated does not have enough time to dissipate into the surrounding environment [21]. The heat generated during deformation processes is modeled by the transient heat conduction given in Eq. (1),

$$\underbrace{\rho c_p \dot{T}}_{\text{temperature rise}} = \underbrace{K_0 \nabla^2 T}_{\text{heat conduction}} - \underbrace{\gamma T_0 \frac{E_{spec}}{1-2\nu} \dot{\epsilon}^e_{kk}}_{\text{thermoelastic effects}} + \underbrace{\beta_{diff} \sigma_{ij} \dot{\epsilon}^p_{ij}}_{\text{thermoplastic effects}} \tag{1}$$

where, $\dot{T}$, T, and T_0, are the heating rate, temperature, and initial temperature, respectively, β_{diff} is the Taylor–Quinney coefficient (i.e., the conversion rate of plastic power to heat), γ, c_p, K_0, and ν are coefficient of thermal expansion, heat capacity, thermal conductivity, and Poisson's ratio, respectively, and $\dot{\epsilon}^e_{kk}$, $\dot{\epsilon}^p_{ij}$ are the elastic and plastic strain-rates. When deformation conditions an be approximated as adiabatic, for instance during high-strain-rate deformation, the conduction term is considered to be zero. A further simplification applied is treating thermoelastic effects as negligible due to them being on the order of a few fractions of degree (≈ 0.2 °C [22]) while the temperature rise due to thermoplastic effects are tens of degrees depending on the material system investigated. These simplifications result in two forms the TQC that are reported in literature, the conversion of plastic power to heat (β_{diff}, see Eq. (2)) and the conversion of plastic work to heat (β_{int}, see Eq. (3)).

$$\beta_{diff} = \frac{\rho c_p \dot{T}}{\sigma_{ij} \dot{\epsilon}^p_{ij}} \tag{2}$$

$$\beta_{int} = \frac{\rho c_p \Delta T}{\int \sigma_{ij} \epsilon^p_{ij}} \tag{3}$$

Table 1
Summary of reported Ti–6Al–4V Taylor–Quinney coefficients.

Reference	Loading mode	Strain rate (s^{-1})	TQC and range	
[31]	Compression	1500	β_{diff}	0.6–0.97
[28]	Compression	2000	β_{int}	0.4–0.5
[28]	Tension	1500–3400	β_{int}	0.3–0.4
[28]	Shear	2800	β_{int}	0.3–0.4
[28]	Shear	5000–7000	β_{int}	0.36–0.45
[32]	Shear	3000	β_{int}	0.4
[33]	Torsion	400	β_{diff}	0.4–1.0
[34]	Torsion	460	β_{diff}	0.2–0.7

The pioneering work of Taylor and coworkers was the first to quantify material's storage capability experimentally [23,24]. Based on their seminal work, the TQC is commonly assumed to be adopt a constant value of ninety-percent, TQC = 0.9. Recent studies have shown the TQC to be dependent on strain (e.g., [25]), strain-rate (e.g., [26,27]), loading mode [28], grain size [29], and active deformation mechanisms [30].

Due to the sensitivity of the TQC to a variety of material and deformation conditions, there is considerable spread in reported values for Ti–6Al–4V in literature. Table 1 presents and overview of reported values. Notably, all of the reported values for the TQC are for Ti–6Al–4V obtained from traditional processing routes. With the prominence that LPBF Ti–6Al–4V has in the area of additively manufactured materials and it being a critical structural alloy, there is a need to obtain an understanding of the TQC for LPBF Ti–6Al–4V in a variety of preparation conditions.

The manuscript is organized as follows. First in section two, experimental methods and specimen preparation are discussed with a specific focus on the optimization of a double Schwarzschild optical system. The inclusion of the optimization process is to provide the thermomechanics community a straightforward approach when selecting an optical system, which in turn is intended to eliminate one possible source of the variability reported in Table 1. Section three presents results pertaining to the microstructure states investigated, their respective dynamic stress–strain behavior as well as their TQC as a function of plastic strain. A discussion is presented pertaining to the possible mechanistic origins of the trends observed in the TQC values of the material systems. Finally, the manuscript closes with a summary of the presented work.

2. Methodology

2.1. Specimen preparation

Wrought specimens used throughout the study were sourced from an annealed high strength grade 5 sheet meeting ASTM B348. The AM specimens investigated in this study were fabricated using Ti–6Al–4V titanium grade 5 powder meeting ASTM F2924 [35]. The LPBF build was performed at the University of Dayton Research Institute (UDRI) Advanced Technology and Training Center on an EOS M290 SLM machine according to the parameters presented in Table 2. Once

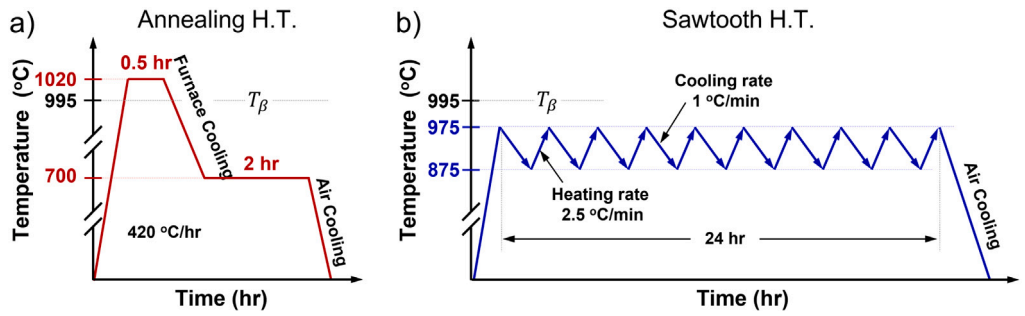

Fig. 1. Schematics of the heat treatments applied to stress-relieved LBPF Ti–6Al–4V (a) Annealing heat treatment exceeding the β-transus temperature [36] (b) Sawtooth heat treatment remaining below the β-transus temperature [37].

Table 2
LPBF print parameters.

Build description	Build specification
Printer type	Laser Powder Bed Fusion (LPBF)
Powder	Ti–6Al–4V titanium grade 5, meets ASTM F2924
Powder vendor	AP and C
Powder size	15–53 μm
Print layer thickness	30 μm
Laser speed	1050 mm/s
Laser power	260 W
Hatch distance	0.14 mm
Strip width	5.00 mm
Stripe overlap	None
Build platform temp	35 °C
Inert gas	Argon

the build was complete, the build plate was subjected to a three hour 913 °C, rapid argon cool, stress relieving heat treatment within a vacuum furnace. Stress-relieved specimens were removed from the build plate using wire electrical discharge machining.

Two heat treatments were utilized to manipulate the LPBF microstructure, one that exceeds the β-phase transus temperature (995 °C) and one that remains below. The first heat treatment, inspired by Ref. [36], utilized a heating rate of 420 °C/h up to a peak temperature of 1020 °C followed by a dwell time of 0.5 h. The furnace was cooled to 700 °C and held for two hours followed by air cooling to room temperature. This first heat treatment acts to eliminate the α' martensitic phase and break up the strong texture of the as-built condition. The second heat treatment, inspired by Ref. [37], utilizes a heating rate of 450 °C/h to reach a temperature of 975 °C. Over the next 24 h, the furnace temperature cycles between 875 °C and 975 °C using a heating rate of 2.5°C/min and cooling rate of 1 °C/min. Once the last cycle is complete, the furnace is allowed to air cool from 975 °C to room temperature. This second heat treatment, referred to throughout as a sawtooth heat treatment, is intended to transition the microstructure from being lath dominated to a globularized structure. Schematic representations of the heat treatments are provided in Fig. 1.

After the heat treatments were completed, specimens were machined to their final dimensions. Specimen geometries and loading orientations with respect to principal processing directions are provided in Fig. 2.

2.2. Microstructure characterization preparation

Specimen surfaces were prepared for Electron Backscatter Diffraction (EBSD) and scanning electron microscope imaging using a three-step grinding process using 180-, 320-, and 600-grit SiC paper followed by three-step polishing using 9 μm and 3 μm polycrystalline diamond and 0.04 μm colloidal silica polishing compounds. After polishing specimens were ultrasonically cleaned in ethanol and finally in distilled water to remove any residual surface particulate. EBSD imaging was conducted at the University of Utah Electron Microscopy Surface Analysis Laboratory on an FEI Teneo SEM equipped with an in lens FeI Trinity ^{TM} detectors utilizing the Velocity^{TM} Super Electron Backscatter Diffraction Camera. EBSD imaging parameters are provided in Table 3. Post acquisition, EBSD data was cleaned using the following steps. The first step is a standardization of the grain confidence index (CI) and fit. In this step, the maximum CI of a grain within each evaluation group or cluster was assigned to the neighboring grains, within that cluster, with the same grain orientation and fit so that all of those grains now have that CI value. The second step is a correlation of the neighboring CI and orientation, where those values were updated for all data points depending on the surrounding points by a statistical voting process. Consequently, from the noise cleaned scans, inverse pole figure (IPF) orientation maps, pole figures (PF) and phase-distribution maps were generated.

2.3. Split-Hopkinson tension bar apparatus

The SHTB setup used consists of an incident bar and transmitted bar both of which are 3.658 m, and a striker tube with a length of 457.2 mm. All bars in the SHTB are made from 350C maraging-steel. Strain gauges in a full-Wheatstone bridge configuration are mounted at the mid-length position to monitor propagating waves. In a SHTB experiment a striker tube impacts a flange on the end of an incident bar generating a tensile wave that travels down the incident bar toward the specimen. The specimen is mounted using a press fit collet system between the incident and transmitted bar. When the propagating tensile wave reaches the specimen, a portion of the wave is transmitted into the specimen, and a portion is reflected backwards toward the impacted flange. A portion of the wave passes through the specimen into the transmitted bar. Raw data traces recorded by the incident bar strain gauges, transmitted bar strain gauges and the IR detector output are shown in Fig. 3. In all experiments copper pulse shapers were used to mechanically filter high frequency content from the propagating waves and to eliminate the need for applying a dispersion correction during one-dimensional wave analysis.

The presence of adiabatic conditions during a SHTB experiment can be confirmed when the experiment's Fourier number ($F_o = \alpha t/l^2$) is less than 0.01 [38]. The loading duration of a SHTB experiment is proportional to the length of the striker tube used and can be considered constant ($t \leq 300$ μs). The gauge length of the specimen ($l = 15.24$ mm) and the thermal diffusivity ($\alpha = 2.87 \times 10^{-6}\ \mathrm{m^2\ s^{-1}}$) of Ti–6Al–4V result in a Fourier number of $3.7{\times}10^{-6}$. Thus, all experiments conducted can be assumed to be adiabatic and the heat conduction term of the transient heat equation (see Eq. (1)) can be approximated as zero.

2.4. Dynamic mechanical behavior assessment

Assuming one-dimensional wave propagation, strain gauge signals are reduced to obtain the specimen's nominal strain-rate, strain, and stress history. Further discussion and derivation of data reduction for

Table 3
EBSD imaging parameters.

Working Distance (WD)	Voltage	Amperage	Sampling step size	Sampling area
12 mm	20 kV	51 nA	1 μm	829 μm at 500X Magnification

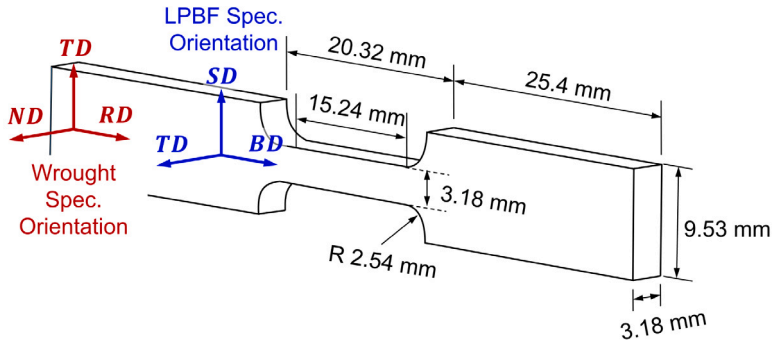

Fig. 2. Schematic of SHTB specimen geometry and loading orientations with respect to principal processing directions used during high-strain-rate IR thermography experiments.

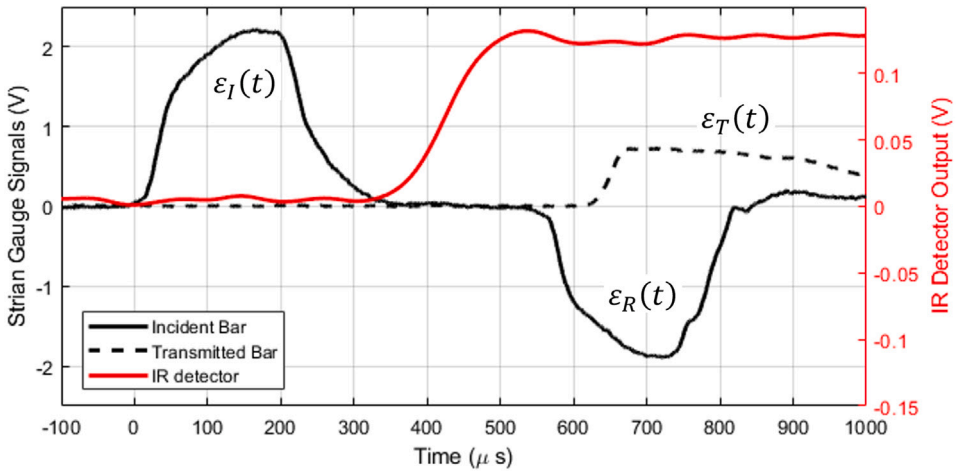

Fig. 3. Typical strain gauge and IR detector signals recorded during a combined SHTB and IR thermography experiment. Portions of the signal used during one-dimensional wave analysis are labeled.

the SHTB can be found elsewhere (e.g., [39–41]). In the following compressive strain is treated as positive. The true strain-rate of the specimen can be written as follows,

$$\dot{\epsilon}^T(t) = \frac{\frac{-2c_0}{L_s}\varepsilon_R(t)}{1 + \int_0^t \frac{2c_0}{L_s}\varepsilon_R(\tau)d\tau} \tag{4}$$

where, c_0 is the bar wave speed, L_s is the specimen gauge length, and $\epsilon_R(t)$ is the reflective wave strain. The true strain of the specimen is obtained through,

$$\epsilon^T(t) = -ln\left[1 + \int_0^t \frac{2c_0}{L_s}\varepsilon_R(\tau)d\tau\right]. \tag{5}$$

Lastly, the specimen's nominal true stress $\sigma_{spec}(t)$ is obtained by

$$\sigma^T(t) = \frac{A_{bar}E_{bar}\varepsilon_T(t)}{t_{spec}w_{spec}}\left[1 + \frac{2c_0}{L_s}\varepsilon_R(t)\right] \tag{6}$$

where, A_{bar} is the bar cross-sectional area, E_{bar} is the bar elastic modulus, $\epsilon_T(t)$ is the transmitted strain, and t_{spec}, w_{spec} are the thickness and width of the specimen's gauge section, respectively.

2.5. Taylor-Quinney coefficient determination

The transient heat conduction equation, presented in Eq. (1), requires taking the time derivative of experimental data to obtain β_{diff}. Due to the sensitivity of time derivatives to experimental noise, the calculation and reporting of β_{int} is favorable and, in general, is more commonly reported. Thus, the TQC was determined using the representation given in Eq. (3). Material properties used to calculate β_{int}, specifically a density of ρ = 4430 kg/m^3 and heat capacity of c_p = 526 J/kg °K where assumed to be identical across the material conditions. No evidence of porosity was observed during EBSD imaging of the LBPF specimens. The SHTB requires multiple wave transits across the specimen prior to one-dimensional wave assumptions being meet. This limitation results in the inability to directly measure low strain properties of materials using the SHTB (e.g., elastic modulus and yield stress using a 0.2% strain offset). Therefore the denominator of Eq. (3) is approximated as the integral of the entire true stress–strain behavior.

2.6. High-speed imaging

The calculation of the TQC is limited to occurring during the portion of material behavior over which deformation is homogeneous. To assess the onset of deformation heterogeneities during deformation that may not be directly evident from the stress–strain behavior (i.e., onset of necking), high speed imaging was incorporated into all experiments. One side of the specimen was speckle patterned using an Iwata Micron B airbrush with acrylic paints while the other was polished with 180 grit SiC paper to achieve consistent surface finish across IR thermography experiments. Images are captured of the deformation process

using a Shimadzu HPVX2 camera equipped with a 100 mm Tokina AT-X Pro lens and a frame rate of 250,000 fps. Specimen illumination was provided by a pair of GS Vitec MultiLED arrays. Image sequences are post processed using commercially available digital image correlation software using the following parameters: subset 23 by 23 pixels; step size 7 pixels; optimized 8-tap interpolation; and zero-normalized squared differences.

2.7. Double-Schwarzschild optical system design and optimization

To record infrared emissions (i.e., temperature rise) from a deforming specimen during a SHTB experiment an infrared detector is often used (e.g., [42]). The view factor (sometimes called configuration factor or shape factor), is the fraction of the energy leaving one object (i.e., specimen) that is intercepted by a second object (i.e., IR detector) [43]. In most cases, it is preferred to increase the view factors using optics rather than proximity of the specimen and IR detector. Newtonian (e.g., [26,30,44–46]), Cassegrain (e.g., [19,20,47]) and double-Schwarzschild (e.g., [48–50]) optical systems are well-known optical configurations for IR thermography. The double Schwarzschild system will be the focus of the following.

The double Schwarzschild optical system consists of two back-to-back Schwarzschild objectives, each operating at an infinite conjugation ratio. Both Schwarzschild objectives consist of a concave mirror with a concentric hole and a convex mirror. In the Schwarzschild optical system, the left and right object-side equivalent focal lengths determine the system's magnification. Schematic illustrations of the Schwarzschild optical system are presented in Fig. 4. Spherical aberrations, coma, and astigmatism are all zero when the ratio of the radii of the convex and concave mirrors is equal to 2.61 [51]. Deviation from this value is not recommended when utilizing sensor arrays, and a ray tracing approach can check the resulting resolution [50]. Additionally, because of the use of mirrors in lieu of lenses, chromatic aberrations are not present. The following presents an approach for designing a double Schwarzschild optical system to achieve high signal to noise ratio for a HgCdTe (MCT) IR detector.

For a single IR detector and mirror based optics, the aforementioned aberrations are not of concern. Therefore, the Schwarzschild objectives can be designed to increase the received emissive power by the IR detector as much as possible (i.e., achieve a high signal-to-noise ratio). For an infinite conjugation factor, the mirror equation for the concave mirror is written as:

$$\frac{1}{a+b}+\frac{1}{f_1+b}=\frac{1}{f_2}, \tag{7}$$

where, a is the distance between the specimen to the convex mirror, b is the distance between the convex mirror to the concave and f_1, f_2, d_1, d_2 are the focal length and diameters of the convex and concave mirrors, respectively. Having considered the spectral radiative energy $dQ_\lambda(S,\Omega,t)$ propagating in direction Ω along path S, the following relationship shows the spectral radiative intensity I_λ.

$$I_\lambda(S,\Omega,t)=\frac{dQ_\lambda(S,\Omega,t)}{dA\,d\lambda\,d\Omega\,dt} \tag{8}$$

where, λ is the emission wavelength, A is the projected area along the path S, Ω is the solid angle, t is time. Assuming the surface of a blackbody, according to Lambert's law, the directional emissive power of a blackbody varies with the cosine of the polar angle. Therefore, one can write the directional emissive power as follows [52,53],

$$E_{\lambda b}(\Theta,\phi)=I_{\lambda b}cos(\Theta). \tag{9}$$

Considering a coaxial area element of radius x and thickness dx (depicted in Fig. 4b), the solid angle subtended by this area element at point P is:

$$d\Omega=\frac{dScos(\Theta)}{(x^2+c^2)}=\frac{2\pi xcdx}{(x^2+c^2)\sqrt{(x^2+c^2)}}. \tag{10}$$

The total emissive power toward the area element can be calculated as $dE_{\lambda b}=I_{\lambda b}\,cos(\theta)d\Omega$. Integrating over all area elements, the following equation provides the total outgoing emissive power from point P received by a disk with diameter R located at a normal distance c from the point. Point P represents the specimen and the disk with a normal distance c and diameter R represent both the concave and convex mirrors.

$$E_{\lambda b,r}=I_{\lambda b}\,\pi\left(1-\frac{c^2}{R^2+c^2}\right) \tag{11}$$

Finally, the efficiency of the Schwarzschild optical system, is calculated using Eq. (12), and can be described as the emissive power received by the concave mirror subtracted by the emissive power blocked by the convex mirror. Eq. (12) has two limiting conditions, the first condition is that of when the convex mirror's diameter is large enough to reflect all of the rays received by the concave mirror, the second condition is that of when the convex mirror's diameter is small so that not all of the rays received by the concave mirror are reflected back by the convex mirror. In the second case, R in Eq. (12) for the concave mirror should be revised to only account for the part of the energy that is being reflected by the convex mirror. Within Eq. (12), $E_{\lambda b,r}$ is the objective function to be optimized. If mirror holders are to be used, the total blocked emissive power will increase and Eq. (12) should be modified according to the mirror holder geometry.

$$\text{if}\quad \frac{f_1+b}{f_1}d_1>d_2:$$

$$E_{\lambda b,r}=\underbrace{\left(1-\frac{(a+b)^2}{d_2^2+(a+b)^2}\right)}_{\text{received by the concave mirror}}-\underbrace{\left(1-\frac{(a+b)^2}{(\frac{a+b}{a})^2d_1^2+(a+b)^2}\right)}_{\text{blocked by the convex mirror}}$$

$$\text{if}\quad \frac{f_1+b}{f_1}d_1<d_2:$$

$$E_{\lambda b,r}=\underbrace{\left(1-\frac{(a+b)^2}{(\frac{f_1+b}{f_1})^2d_1^2+(a+b)^2}\right)}_{\text{received by the effective concave mirror}}-\underbrace{\left(1-\frac{(a+b)^2}{(\frac{a+b}{a})^2d_1^2+(a+b)^2}\right)}_{\text{blocked by the convex mirror}} \tag{12}$$

To select components for the Schwarzschild system, the optical parameters of gold coated concave and convex mirrors were extracted from the catalogs of different manufacturers. Gold was selected for the mirror coating due to it have a reflectivity greater than 96 percent over the entire 2–15 μm range that the HgCdTe MCT IR detector is sensitive. The distance between the specimen to the convex mirror a is selected based on requirements for calibration procedures and field of view considerations. Having all necessary parameters, and solving Eq. (7), the separation distance of the concave and convex mirrors (b) were calculated to ensure an infinite conjugation factor. Thereafter, the objective function was computed for 180 possible designs. The constructed system, consisting of CM750-075-M01 concave mirrors from Thorlabs with a 12.7 mm diameter through hole, and 64-071 convex mirrors from Edmund optics is shown in Fig. 5. The efficiency of the range of possible designs is presented in Fig. 5, with the selected design highlighted in red. Within Fig. 5 some designs are shown as having zero efficiency, this is due to either the mirror equation not being solvable or that the efficiency was negative indicating the emissive power blocked by the convex mirror was greater than the emissive power captured by the concave mirror. The mirror equation (Eq. (7)) cannot be solved for b when f_1 is very small relative to f_2 and a. Therefore, when $1/f_2 > 1/f_1+1/a$, for no positive value of b is Eq. (7) solvable. Experimental considerations, specifically field of view, clear apertures of the mirrors, working distance, proximity of the mirrors to the SHTB (e.g., to allow for the placement of a chopping wheel), and mirror spacing, as well as cost resulted to the selection of an optical system that is slightly below the optimal case. A key benefit of the double Schwarzschild design

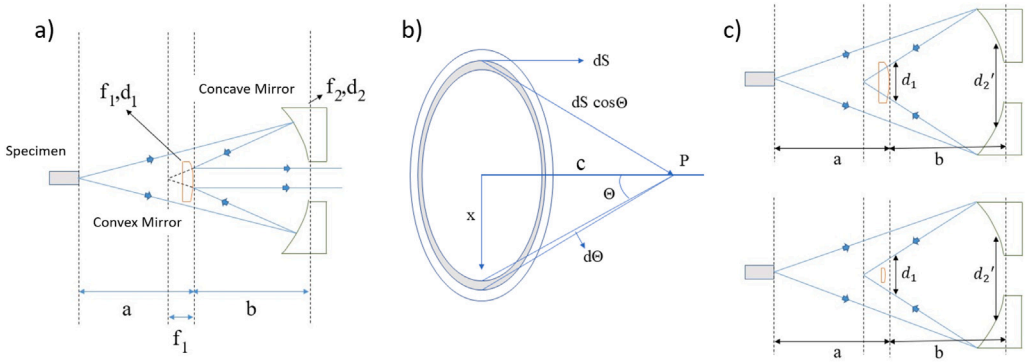

Fig. 4. Overview of the Schwarzschild optical system design, (a) single Schwarzschild objective parameters, (b) intensity received by a coaxial element and (c) double Schwarzschild objective parameters.

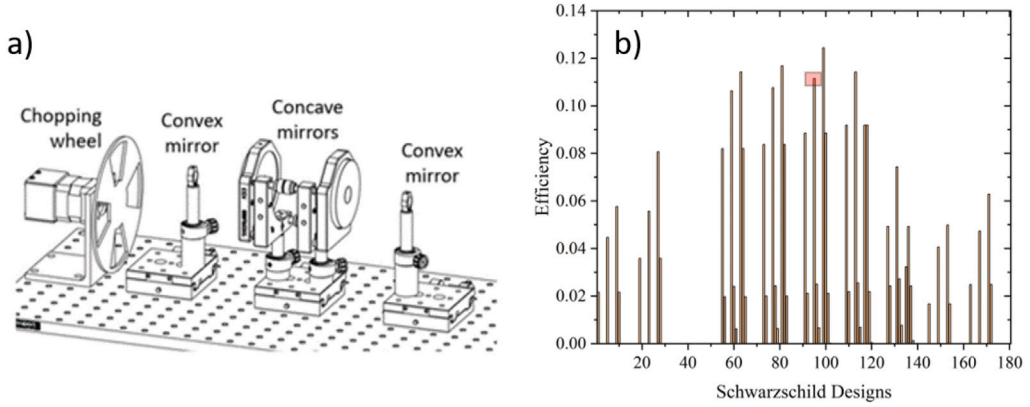

Fig. 5. CAD model of the designed and built double Schwarzschild optical system and (b) efficiency of possible designs. The selected design is highlighted in red.

is that once aligned, illumination of the specimen during high speed imaging does not contaminate the recorded IR signal. Other commonly used optical systems, such as the Newtonian optical system, do not have this benefit.

2.8. IR detector calibration

An IR detector calibration process is adopted to obtain the relationship between the IR detector output voltage and the interrogated specimen temperature. In this process a specimen is mounted in the SHTB system, heated, and allowed to cool to room temperature. The specimen temperature during the cooling process is monitored by a thermocouple embedded near the specimen surface. A chopping wheel is used to provide a dynamic signal to the IR detector as it records the specimen cooling. Fig. 6 shows the results from two calibration experiments. Over the range of temperatures that are expected during an experiment the curves are nominally identical.

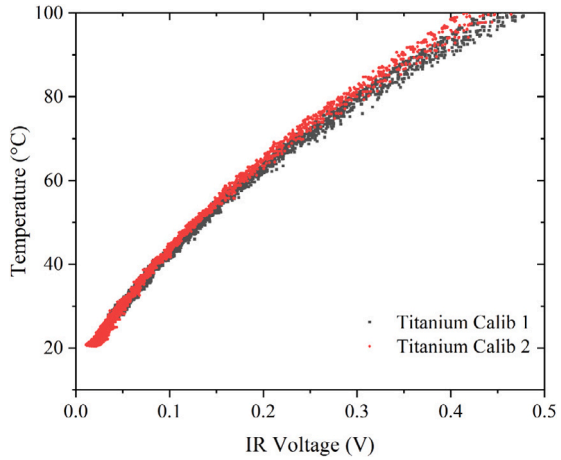

Fig. 6. Calibration curves.

3. Results

3.1. Microstructure

Three Ti–6Al–4V material conditions were examined, specifically annealed Ti–6Al–4V rolled sheet (grade 5), and stress relieved LPBF Ti–6Al–4V subjected to either a heat treatment above the β-transus temperature or a sawtooth heat treatment below the β-transus temperature. Figs. 7 through 9 present EBSD derived inverse pole figure orientation maps, phase distributions (i.e., percentage α-phase vs. β-phase, and α-phase pole figure triads. Porosity was not readily observed in either of the LPBF materials.

The wrought material condition consists of equiaxed grains with an average diameter of 5 μm. The phase distribution map finds the microstructure to be 85.9% α-phase and 14.1% β-phase. As expected a strong texture is present with the [0001] pole being oriented closely to the normal processing direction.

The annealing heat treatment microstructure presents with a characteristic lath structure with large aspect ratio lenticular grains whose average width and length are 13 μm and 98 μm, respectively, for an aspect ratio of 7.5. The phase distribution map finds an almost entirely alpha-phase microstructure with more than 98.5% of the observed area being alpha-phase and less than 1.5% being beta phase. The pole figure triad shows a relatively random texture has been achieved. Exceeding the β-transus temperature has sufficiently transformed any α'-phase

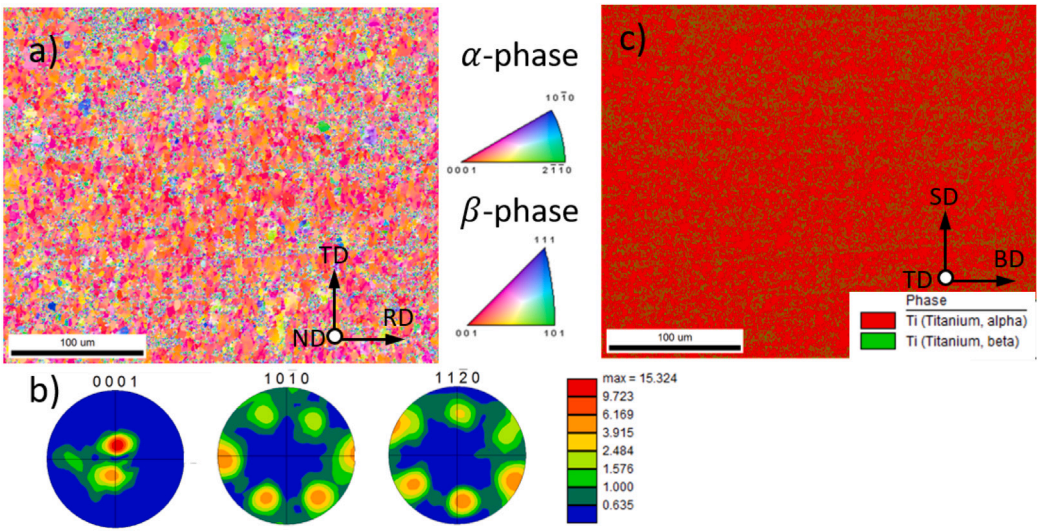

Fig. 7. Overview of the wrought material condition (a) inverse pole figure obtained with a reference direction matching the normal principle processing direction (out-of-page), (b) α-phase pole figure triad, (c) α and β phase distribution showing an α-phase dominated microstructure (85.9% α-phase).

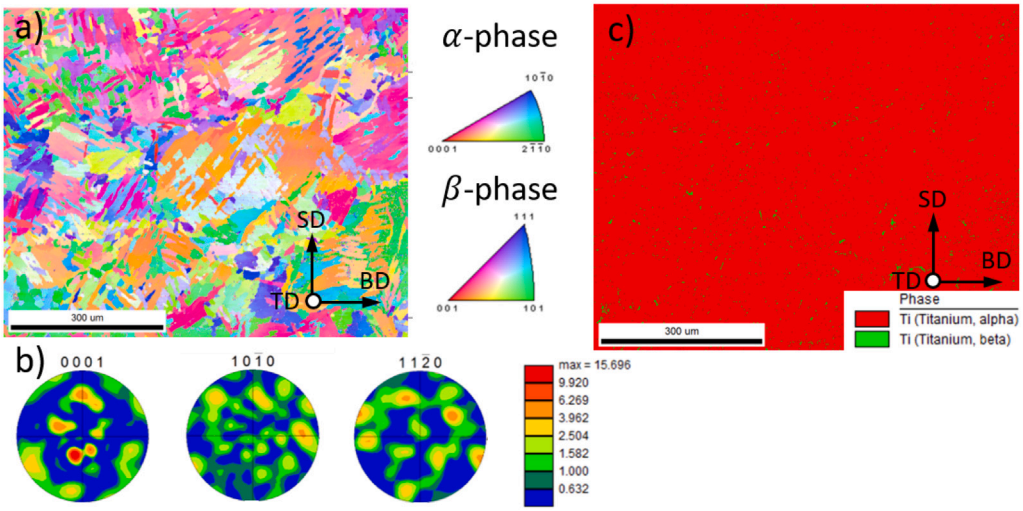

Fig. 8. Overview of the annealing heat treatment material condition, (a) inverse pole figure obtained with a reference direction matching the transverse principle processing direction (out-of-page), (b) α-phase pole figure triad, (c) α and β phase distribution showing an α-phase dominated microstructure (98.5% α-phase).

martensitic laths into the β-phase which upon cooling, became α-phase lamella surrounded by β-phase grains.

The sawtooth heat treatment can be observed to also present with the characteristic lath structure. The sawtooth, or globularization heat treatment is an attempt to achieve the equiaxed or bimodal structure. Compared to the annealed heat treatment, there has been a decrease in the lenticular grain aspect ratio and general growth of the lenticular grains in the thickness direction while contracting in their length direction. Lenticular grains were found to have an average thicknesses of 22 μm and lengths of 68 μm, respectively, for an aspect ratio of 3.10. It is evident from the IPF that an incomplete globularization process has occurred. During the globularization process the thermal cycling causes oscillations in the volume fractions of α and β phases that in synergism with the slow cooling segments of the cycle globularize the α phase by epitaxial growth [37]. Here bimodal refers to a microstructure comprised of equiaxed primary α grains and transformed β areas, which surround the alpha grains, can be regarded as a kind of "dual-phase" structure [54]. Research suggests that when α'-phase martensite decomposes during the globularization heat treatment, the α-phase will be first nucleated within the acicular α'-phase following an expected recovery mechanism [55,56]. During this process, vanadium diffuses from the newly formed α-phase and concentrates at the α-phase boundary [55,56]. This element partitioning then leads to the formation of β-phase in the vanadium-rich area between α lamellae [55,56]. The phase distribution map shown in Fig. 9 provide clear indication of partitioning having taken place. The sawtooth profile has a comparatively large amount of β-phase (89.1% α and 10.9% β) when compared to the annealing heat treatment.

3.2. Dynamic behavior

To determine the onset of necking, which in turn provides the plastic strain level that the TQC can be calculated, the axial strain of a deforming specimen was determined for each of the 128 images captured during an experiment or up to specimen fracture. Fig. 10 provides the axial strain evolution of a nominally representative specimen from each material condition. The vertical dashed red line corresponds to the position along the gauge length interrogated by the IR detector. Time zero corresponds to the horizontal axis and time increases when moving in the vertical direction. For clarity, the strain distribution of every 16th frame is shown as a dashed black line. For each material condition

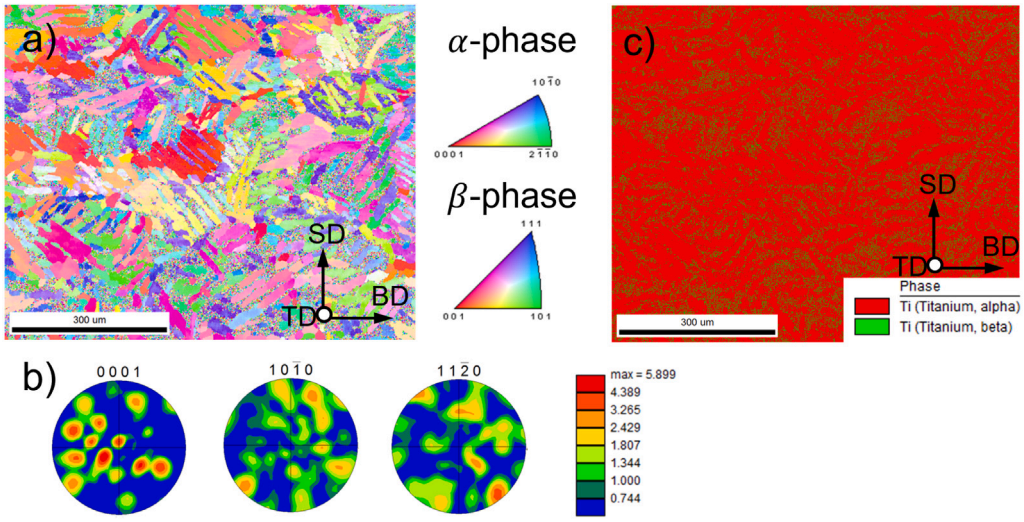

Fig. 9. Overview of the sawtooth heat treatment material condition, (a) inverse pole figure obtained with a reference direction matching the transverse principle processing direction (out-of-page), (b) α-phase pole figure triad, (c) α and β phase distribution showing an α-phase dominated microstructure (89.1% α-phase).

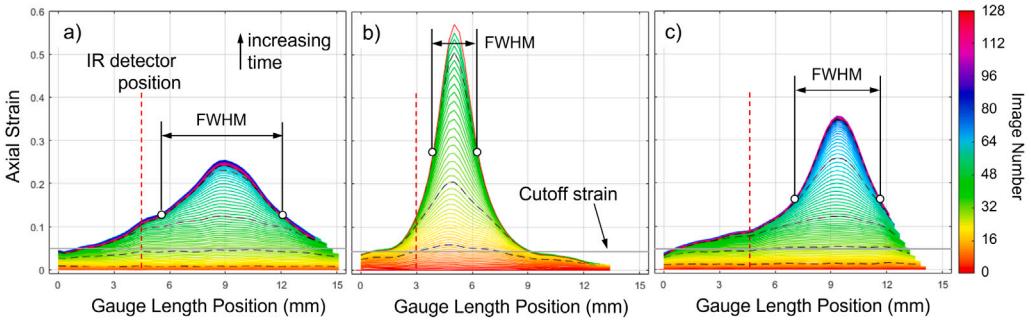

Fig. 10. Axial strain evolution derived from DIC analysis for necking identification of the (a) wrought, (b) annealed LPBF, and (c) sawtooth LPBF material conditions.

the accumulation of strain is nominally homogeneous across the gauge section during the early stages of deformation. Cut-off strains, indicated by a gray horizontal line, of 5%, 4% and 4.5%, were determined for the wrought, annealed an globularized material conditions, respectively. While TQC values for material conditions are included over the entirely of the true stress–strain behavior they should only be accepted as valid up to the cut-off strain (i.e., the end of homogeneous deformation).

Once necking occurs it is evident that strain accumulates in the necking region until specimen failure. The width of the necking region was quantitatively assess by determining the full-width half maximum (FWHM) of the strain distribution of the image of the loading sequence or in the case of the annealed LPBF material from the last frame before fracture. It is evident that among the three conditions, the necking region is the most diffuse in the wrought condition (width of ≈ 7 mm), followed by the globularized condition (width of ≈ 4.5 mm), and was most concentrated in the annealed condition (width of ≈ 2.5 mm).

Triplicate TSPHB experiments combined with in-situ IR thermography were conducted on each material preparation condition. The true stress–strain behavior and corresponding temperature rise of each experiment are reported in Fig. 11. Consistent and repeatable behavior was observed across the three specimen replicates. The yield strength for wrought, annealed, and globularized specimens was 1350 MPa, 1250 MPa, 1200 MPa respectively and all had a near zero strain hardening behavior. The vertical black dashed lines indicate the cut-off strain for TQC analysis. In general, measured temperatures are in agreement up to the cut-off strain after which the diverge. This diverging behavior should be expected as the stress–strain behavior derived from one-dimensional analysis no longer is in agreement with the local state of strain.

3.3. Thermomechanical characterization

The evolution of the TQC as a function of plastic strain is presented in Fig. 12. For the wrought condition, in addition to the three replicate experiments, data from literature is also included, specifically the work of Rittel et al. [28]. It is observed that their TQC data agrees well with the TQC values obtained under dynamic tension. Interestingly the near zero strain hardening results in near constant conversion of plastic work to heat conversion for the wrought condition but does not for the annealed and the globularized conditions. In the annealed condition, the TQC rapidly increases during homogeneous deformation leading up to the cut-off strain after which values diverge. The globularized microstructure exhibits increasing efficiency of the plastic work to heat conversion and appears to begin to plateau at the later stages of homogeneous deformation.

In some situations, it may be favorable to have a single value approximation of the TQC during homogeneous deformation, β_{int}^{avg}. The single value is found by plotting the heat density ($\rho c_p \Delta T$) vs. work density for each experiment up to the respective cut-off strain. A linear fit is applied to the three experiments and its slope is determined. This single value can be approached as an estimate of the average TQC for deformation. Wrought was found to have the lowest TQC ($\beta_{int} = 0.35$), following by the globularized condition ($\beta_{int} = 0.52$), and the annealed condition showed the greatest TQC ($\beta_{int} = 0.75$). $\beta_{int} = 0.52$ (see Fig. 13).

4. Discussion

The microstructure state of each of the material conditions will have a direct impact on the deformation mechanism activity. In dual

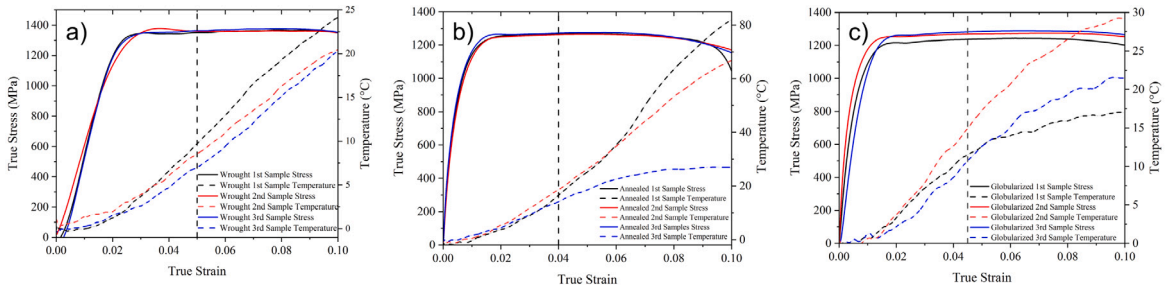

Fig. 11. True stress–strain curves vs. temperature rise for the (a) wrought specimens at nominal strain rate of 700 s^{-1} (b) annealed heat treatment specimens at a nominal strain rate of 760 s^{-1}, and (c) sawtooth heat treatment specimens at a nominal strain rate of 730 s^{-1}.

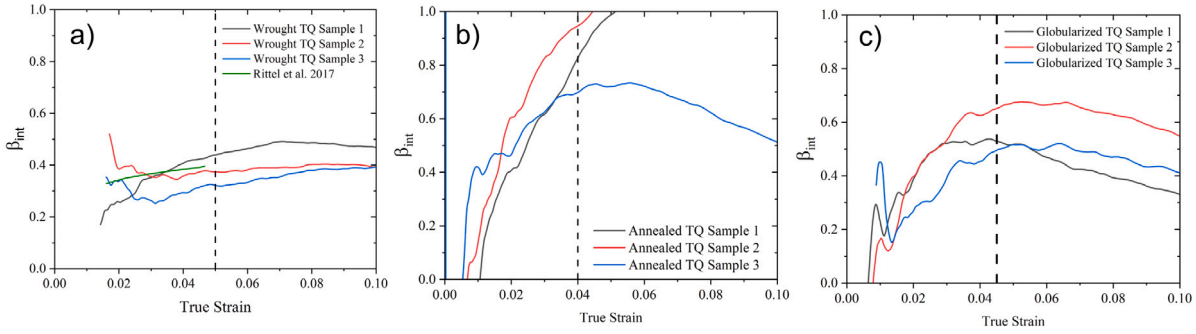

Fig. 12. TQC as a function of strain for (a) wrought specimens at nominal strain rate of 700 s^{-1} (b) annealed specimens at a nominal strain rate of 760 s^{-1}, and (c) globularized specimens at a nominal strain rate of 730 s^{-1}.

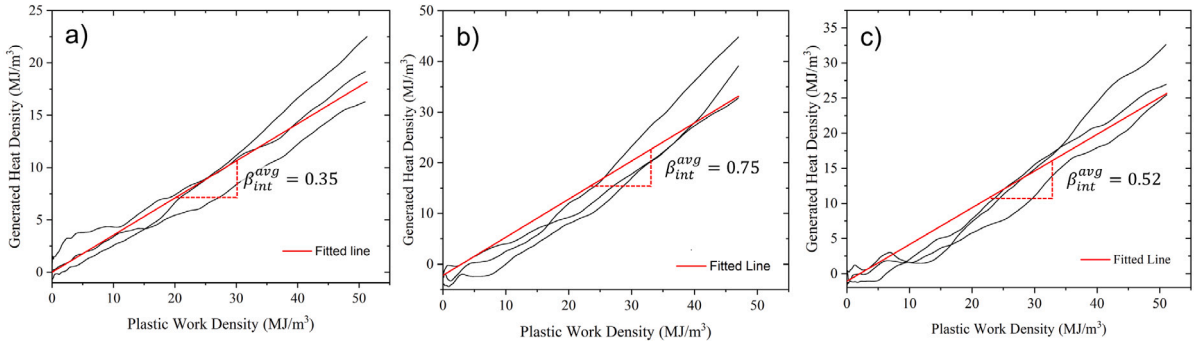

Fig. 13. Single value approximation of the TQC for (a) wrought, (b) annealed heat treatment and (c) sawtooth heat treatment determined from the linear fit applied up to the cut-off strain for each.

phase titanium alloys (i.e., Ti–6Al–4V), deformation twinning is generally considered to be inhibited due to high solute content [57,58]. However, recent work has demonstrated deformation twining to be an active deformation mechanism in Ti–6Al–4V (e.g., [59,60]). Coghe et al. investigated the activation of twinning as a function of strain-rate. In an equiaxed grain structure closely matching the wrought condition investigated here, $\{10\bar{1}2\}\langle\bar{1}011\rangle$ twins were observed via TEM and EBSD. Twinning fractions present were found to be loading orientation and strain rate dependent. Over the dynamic regime, twin fractions approaching to 5% were observed [59]. Due to the conflicting stances in literature as well as the limited presence of deformation twinning in Ti–6Al–4V, dislocation slip is considered to be the primary deformation mode in this dual-phase titanium alloy. While twinning could be expected to occur in the wrought condition particularly at elevated strain-rates, its effect on the observed TQC is thought to be second order effect. Previous studies that have examined the TQC of hcp alloy Mg AZ321B, found when plasticity is accommodated through deformation twins the TQC is suppress compared to slip dominated processes [30].

The strong texture of the wrought material places the c-axis of most grains perpendicular to the loading access. In this loading orientation deformation processes will be accommodated through dislocation slip mechanisms whose Burgers vector is resolved along the $\langle a\rangle$ direction. These slip mechanisms include prismatic $(10\bar{1}0)\langle11\bar{2}0\rangle$, basal $(0001)\langle11\bar{2}0\rangle$, and first order pyramidal $\langle a\rangle$ slip $(10\bar{1}1)\langle11\bar{2}0\rangle$ [61]. Among these three mechanisms, basal and prismatic slip have lower critical resolved shear stress required for activation (e.g., [62–64]). Additionally, the strong texture of the wrought material results in neighboring α-phase grains having closely matching orientations which provides well aligned pathways for slip transfer across grain boundaries [61] as well as similar schmid factors across a large number of grains. Combined these lead to easy slip transfer [65]. For grain sizes and loading orientations similar to those used here, slip trace analysis observed deformation predominantly occurs through a combination of low CRSS systems, specifically prismatic $\langle a\rangle$ slip and basal $\langle a\rangle$ slip mechanisms [66]. It is thought that the wrought condition presents with the lowest TCQ due to the well aligned slip systems across neighboring grains with similar orientations and the ease of activation of accommodating deformation mechanisms. As a greater portion of the work of deformation is stored within the microstructure through

dislocation-based processes, less will be converted into heat and a lower TQC would be expected.

EBSD analysis of the annealed microstructure observed adjacent laths to have significant misorientation. This misorientation results in more difficult slip transfer processes across interfaces. When slip is hindered, dislocation pile-ups at these interfaces are likely to occur. This coupled with the limited mean free path of dislocations across the lath width could provide a greater number of dislocation-boundary and dislocation–dislocation interactions. These interactions in turn reduce the efficiency of storing the work of deformation which results in the greatest TQC among the material conditions investigated.

Lastly, the globularized microstructure has a combination of features of the other two microstructures, specifically the lenticular α-phase and surrounding β-phase. The interface of the α-phase/β-phase has an established Burgers orientation relationship (BOR), where $(0001)_\alpha \parallel (110)_\beta$ and $\langle 11\bar{2}0\rangle_\alpha \parallel \langle 111\rangle_\beta$. Under slow cooling rates, the BOR has been observed throughout lamellar microstructures. However, if cooling rates are rapid, deviations from this BOR have been are possible (e.g., [67]). Considering that the sawtooth heat treatment used remains below the β-phase transus temperature, it is possible that residual regions deviating from the BOR could be present as a direct result of the rapid cooling process involved in LPBF. Deviations from the BOR would provide a barrier to dislocation motion. The possibility of deviations from the BOR provides a feasible explanation as to why there would be an increase in the TQC of the globularized condition compared to the wrought condition. Future work aims to provide an detailed TEM investigation of the interaction of slip mediated process with $\alpha - \beta$ interfaces, specifically those deviating from the BOR, within the globularized microstructure.

5. Summary

This paper reports a systematic study of the plastic work to heat conversion of the importation aerospace alloy Ti–6Al–4V, and the optimization of the double Schwarzschild optical system. The particular benefit of using the double Schwarzschild optical system is the incorporation of high speed imaging without lighting sources contaminating IR thermography measurements. Three preparation conditions were investigated, namely the wrought condition in an annealed form, and stress-relieved LPBF subjected to an annealing heat treatment exceeding the beta-transus temperature, or to a sawtooth profile below the β-transus temperature. Each of the material systems demonstrated a Taylor–Quinney coefficient below the commonly held assumption of 0.9. The importance of interface orientation is discussed with easy slip transfer interfaces resulting in a lower TQC than material conditions with interfaces that present as stronger barriers to dislocations processes. From a practical standpoint, the generated TQC data provides a starting point for the establishment of a database of the work to heat conversion efficiency of for this critical AM LPBF alloy.

CRediT authorship contribution statement

Seyyed-Danial Salehi: Formal analysis, Investigation, Writing – original draft, Visualization. **Roger Beal:** Investigation, Visualization, Writing – original draft. **Owen T. Kingstedt:** Conceptualization, Resources, Writing – review & editing, Project administration, Funding acquisition.

Declaration of competing interest

The authors declare that they have no known competing financial interests or personal relationships that could have appeared to influence the work reported in this paper.

Data availability

Data will be made available on request.

Acknowledgments

This research was supported in part by the National Science Foundation, United States through CAREER award no. 1847653. A portion of the presented work made use of University of Utah shared facilities of the Micron Technology Foundation Inc. Microscopy Suite sponsored by the College of Engineering, Health Sciences Center, Office of the Vice President for Research, and the Utah Science Technology and Research (USTAR), United States initiative of the State of Utah. The additively manufactured Ti–6Al–4V specimens were provided by the University of Dayton Research Institute (UDRI), with special thanks to Thad Kacsandy of UDRI for all of his assistance in the specimen manufacture and heat treatment. The authors would like to acknowledge the Air Force Life Cycle Management Center Product Support Engineering Division, Ms. Debra Naguy and Mr. Matthew Phillips, for funding the material specimen production and the Air Force STEM+M program for sponsoring Roger Beal. The authors would like to thank Dr. Paulo Perez and Dr. Brian Van Devener from surface analysis lab at University of Utah Nanofab for their assistance in equipment operation and training. Additionally, a portion of this work was performed in part at the Utah Nanofab sponsored by the College of Engineering, Office of the Vice President for Research, and the Utah Science Technology and Research (USTAR), United States initiative of the State of Utah. The author(s) appreciate the support of the staff and facilities that made this work possible.

References

[1] Inagaki I, Takechi T, Shirai Y, Ariyasu N. Application and features of titanium for the aerospace industry. 2014.
[2] Alaghmandfard R, Dharmendra C, Odeshi AG, Mohammadi M. Dynamic mechanical properties and failure characteristics of electron beam melted Ti-6Al-4V under high strain rate impact loadings. Mater Sci Eng A 2020;793:139794.
[3] DebRoy T, Wei HL, Zuback JS, Mukherjee T, Elmer JW, Milewski JO, Beese AM, Wilson-Heid A, De A, Zhang W. Additive manufacturing of metallic components – Process, structure and properties. Prog Mater Sci 2018;92:112–224.
[4] Liu S, Shin YC. Additive manufacturing of Ti6Al4V alloy: A review. Mater Des 2019;164:107552.
[5] Cao S, Zou Y, Lim CVS, Wu X. Review of laser powder bed fusion (LPBF) fabricated Ti-6Al-4V: process, post-process treatment, microstructure, and property. Light: Adv Manuf 2021;2:313.
[6] Mishurova T, Evsevleev S, Artzt K, Haubrich J, Sevostianov I, Requena G, Bruno G. Micromechanical behavior of annealed Ti-6Al-4V produced by laser powder bed fusion. Eur J Mater 2022;2(1):186–200.
[7] Simonelli M, Tse YY, Tuck C. On the texture formation of selective laser melted Ti-6Al-4V. Metall Mater Trans A 2014;45:2863–72.
[8] Agius D, Kourousis KI, Wallbrink C, Tingting S. Cyclic plasticity and microstructure of as-built SLM Ti-6Al-4V: The effect of build orientation. Mater Sci Eng A 2017;85–100.
[9] Cao S, Zou Y, Lim CVS, Wu X. Review of laser powder bed fusion (LPBF) fabricated Ti-6Al-4V: process, post-process treatment, microstructure, and property. Light: Adv Manuf 2021;2(313).
[10] Huang Q, Liu X, Yang X, Zhang R, Shen Z, Feng Q. Specific heat treatment of selective laser melted Ti–6Al–4V for biomedical applications. Front Mater Sci 2015;9:373–81.
[11] Vrancken B, Thijs L, Kruth J-P, Van Humbeeck J. Heat treatment of Ti6Al4V produced by selective laser melting: Microstructure and mechanical properties. J Alloys Compd 2012;541:177–85.
[12] Grimm T, Wiora G, Witt G. Characterization of typical surface effects in additive manufacturing with confocal microscopy. Surf Topogr: Metrol Prop 2015;3(1):014001.
[13] Leary M. Surface roughness optimisation for selective laser melting (SLM): Accommodating relevant and irrelevant surfaces. In: Laser additive manufacturing. Woodhead publishing series in electronic and optical materials, Woodhead Publishing; 2017, p. 99–118.
[14] Nakatani M, Masuo H, Tanaka Y, Murakami Y. Effect of surface roughness on fatigue strength of Ti-6Al-4V alloy manufactured by additive manufacturing. Procedia Struct Integr 2019;19:294–301, Fatigue Design 2019, International Conference on Fatigue Design, 8th Edition.
[15] Jiménez A, Bidare P, Hassanin H, Tarlochan F, Dimov S, Essa K. Powder-based laser hybrid additive manufacturing of metals: a review. Int J Adv Manuf Technol 2021;114.
[16] Sefene EM, Asmare A. Metal hybrid additive manufacturing: state-of-the-art. Prog Addit Manuf 2022.

[17] Abukhshim N, Mativenga P, Sheikh M. Heat generation and temperature prediction in metal cutting: A review and implications for high speed machining. Int J Mach Tools Manuf 2006;46:782–800.

[18] Sela A, Ortiz de Zarate G, Soler D, Germain G, Gallegos L, Arrazola P. Adiabatic self-heating determination for Ti6al4v at different temperatures. SSRN Electron J 2022.

[19] Guo Y, Ruan Q, Zhu S, Wei Q, Lu J, Hu B, Wu X, Li Y. Dynamic failure of titanium: Temperature rise and adiabatic shear band formation. J Mech Phys Solids 2020;135:103811.

[20] Guo Y, Ruan Q, Zhu S, Wei Q, Chen H, Lu J, Hu B, Wu X, Li Y, Fang D. Temperature rise associated with adiabatic shear band: causality clarified. Phys Rev Lett 2019;122(1):015503.

[21] Soares GC, Hokka M. The Taylor–Quinney coefficients and strain hardening of commercially pure titanium, iron, copper, and tin in high rate compression. Int J Impact Eng 2021;156:103940.

[22] Bever MB, Holt DL, Titchener AL. The stored energy of cold work. Prog Mater Sci 1973;17:5–177.

[23] Farren WS, Taylor GI. The heat developed during plastic extension of metals. Proc R Soc A 1925;107.

[24] Taylor GI, Quinney H. The latent energy remaining in a metal after cold working. Proc R Soc A 1934;143:307–26.

[25] Hodowany J, Ravichandran G, Rosakis AJ, Rosakis P. Partition of plastic work into heat and stored energy in metals. Exp Mech 2000;40(2):113–23.

[26] Ghosh D, Kingstedt OT, Ravichandran G. Plastic work to heat conversion during high-strain rate deformation of Mg and Mg alloy. Metall Mater Trans A 2017;48(1):14–9.

[27] Soares GC, Hokka M. The Taylor–Quinney coefficients and strain hardening of commercially pure titanium, iron, copper, and tin in high rate compression. Int J Impact Eng 2021;156:103940.

[28] Rittel D, Zhang LH, Osovski S. The dependence of the Taylor–Quinney coefficient on the dynamic loading mode. J Mech Phys Solids 2017;107:96–114.

[29] Oliferuk W, Korbel A, Grabski MW. Mode of deformation and the rate of energy storage during uniaxial tensile deformation of austenitic steel. Mater Sci Eng A 1996;220(1–2):123–8.

[30] Kingstedt OT, Lloyd JT. On the conversion of plastic work to heat in Mg alloy AZ31B for dislocation slip and twinning deformation. Mech Mater 2019;134:176–84.

[31] Mason JJ, Rosakis AJ, Ravichandran G. On the strain and strain rate dependence of the fraction of plastic work converted to heat: an experimental study using high speed infrared detectors and the Kolsky bar. Mech Mater 1994;17(2–3):135–45.

[32] Rittel D, Wang ZG. Thermo-mechanical aspects of adiabatic shear failure of AM50 and Ti6Al4V alloys. Mech Mater 2008;40(8):629–35.

[33] Macdougall D. Determination of the plastic work converted to heat using radiometry. Exp Mech 2000;40(3):298–306.

[34] Macdougall DAS, Harding J. The measurement of specimen surface temperature in high-speed tension and torsion tests. Int J Impact Eng 1998;21(6):473–88.

[35] Standard ASTM. Specification for additive manufacturing titanium-6 aluminum-4 vanadium with powder bed fusion. West Conshohocken, PA, USA: ASTM International; 2014.

[36] K. Punit, R. Upadrasta. Microstructural optimization through heat treatment for enhancing the fracture toughness and fatigue crack growth resistance of selective laser melted Ti6Al4V alloy. Acta Mater 2019;169:45–59.

[37] Sabban R, Bahl S, Chatterjee K, Suwas S. Globularization using heat treatment in additively manufactured Ti-6Al-4V for high strength and toughness. Acta Mater 2019;162:239–54.

[38] Zehnder AT, Babinsky E, Palmer T. Hybrid method for determining the fraction of plastic work converted to heat. Exp Mech 1998;38(4):295–302.

[39] Chen WW, Song B. Split Hopkinson (Kolsky) bar: Design, testing and applications. Springer Science & Business Media; 2010.

[40] Gama BA, Lopatnikov SL, Gillespie Jr JW. Hopkinson bar experimental technique: a critical review. Appl Mech Rev 2004;57(4):223–50.

[41] Ramesh KT. High rates and impact experiments. In: Sharpe William N, editor. Springer handbook of experimental solid mechanics. Boston, MA: Springer US; 2008, p. 929–60.

[42] Gao C, Iwamoto T. Measurement of transient temperature at super-high-speed deformation. Int J Mech Sci 2021;206:106626.

[43] Lienhard IV, John H. A heat transfer textbook. phlogiston Press; 2005.

[44] Varga J, Kingstedt OT. An investigation of the plastic work to heat conversion of wrought and laser powder bed fusion manufactured Inconel 718. Addit Manuf 2021;46:102179.

[45] Vernaza-Pena KM, Mason JJ, Li M. Experimental study of the temperature field generated during orthogonal machining of an aluminum alloy. Exp Mech 2002;42(2):221–9.

[46] Ravichandran G, Rosakis AJ, Hodowany J, Rosakis P. On the conversion of plastic work into heat during high-strain-rate deformation. In: AIP conference proceedings, Vol. 620. American Institute of Physics; 2002, p. 557–62.

[47] Zehnder AT, Rosakis AJ. On the temperature distribution at the vicinity of dynamically propagating cracks in 4340 steel. J Mech Phys Solids 1991;39(3):385–415.

[48] Nieto-Fuentes JC, Rittel D, Osovski S. On a dislocation-based constitutive model and dynamic thermomechanical considerations. Int J Plast 2018;108:55–69.

[49] Guduru PR, Rosakis AJ, Ravichandran G. Dynamic shear bands: an investigation using high speed optical and infrared diagnostics. Mech Mater 2001;33(7):371–402.

[50] Zehnder AT, Guduru PR, Rosakis AJ, Ravichandran G. Million frames per second infrared imaging system. Rev Sci Instrum 2000;71(10):3762–8.

[51] Kingslake R, Johnson B. Lens design fundamentals. academic Press; 2009.

[52] Modest MF, Mazumder S. Radiative heat transfer. Academic Press; 2021.

[53] Arecchi AV, Koshel RJ, Messadi T. Field guide to illumination. SPIE; 2007.

[54] Chong Y, Bhattacharjee T, Park M-H, Shibata A, Tsuji N. Factors determining room temperature mechanical properties of bimodal microstructures in Ti-6Al-4V alloy. Mater Sci Eng A 2018;730:217–22.

[55] Zou Z, Simonelli M, Katrib J, Dimitrakis G, Hague R. Microstructure and tensile properties of additive manufactured Ti-6Al-4V with refined prior-β grain structure obtained by rapid heat treatment. Mater Sci Eng A 2021;814:141271.

[56] Zhang X-Y, Fang G, Leeflang S, Böttger AJ, Zadpoor AA, Zhou J. Effect of subtransus heat treatment on the microstructure and mechanical properties of additively manufactured Ti-6Al-4V alloy. J Alloys Compd 2018;735:1562–75.

[57] Zaefferer S. A study of active deformation systems in titanium alloys: dependence on alloy composition and correlation with deformation texture. Mater Sci Eng A 2003;344(1–2):20–30.

[58] Williams JC, Baggerly RG, Paton NE. Deformation behavior of HCP Ti-Al alloy single crystals. Metall Mater Trans A 2002;33(3):837–50.

[59] Coghe F, Tirry W, Rabet L, Schryvers D, Van Houtte P. Importance of twinning in static and dynamic compression of a Ti–6Al–4V titanium alloy with an equiaxed microstructure. Mater Sci Eng A 2012;537:1–10.

[60] Zheng X, Zheng S, Wang J, Ma Y, Wang H, Zhou Y, Shao X, Zhang B, Lei J, Yang R, Ma X. Twinning and sequential kinking in lamellar Ti-6Al-4V alloy. Acta Mater 2019;181:479–90.

[61] Bridier F, Villechaise P, Mendez J. Analysis of the different slip systems activated by tension in a α/β titanium alloy in relation with local crystallographic orientation. Acta Mater 2005;53(3):555–67.

[62] Mayeur JR, McDowell DL. A three-dimensional crystal plasticity model for duplex Ti–6Al–4V. Int J Plast 2007;23(9):1457–85.

[63] Semiatin SL, Bieler TR. The effect of alpha platelet thickness on plastic flow during hot working of Ti–6Al–4V with a transformed microstructure. Acta Mater 2001;49(17):3565–73.

[64] Benmessaoud F, Cheikh M, Velay V, Vidal V, Matsumoto H. Role of grain size and crystallographic texture on tensile behavior induced by sliding mechanism in Ti-6Al-4V alloy. Mater Sci Eng A 2020;774:138835.

[65] Guo Y, Britton TB, Wilkinson AJ. Slip band–grain boundary interactions in commercial-purity titanium. Acta Mater 2014;76:1–12.

[66] Benmessaoud F, Cheikh M, Velay V, Vidal V, Matsumoto H. Role of grain size and crystallographic texture on tensile behavior induced by sliding mechanism in Ti-6Al-4V alloy. Mater Sci Eng A 2020;774:138835.

[67] Jha JS, Toppo SP, Singh R, Tewari A, Mishra SK. Deformation behavior of Ti-6Al-4V microstructures under uniaxial loading: Equiaxed vs. transformed-β microstructures. Mater Charact 2021;171:110780.